Research Article

Novel transparent MgGa$_2$O$_4$ and Ni^{2+}-doped MgGa$_2$O$_4$ ceramics

Guangran ZHANG^a, Adrian GOLDSTEIN^b, Yiquan WU^{a,*}

^{a}*Kazuo Inamori School of Engineering, New York State College of Ceramics, Alfred University, Alfred, New York 14802, USA*
^{b}*Israel Ceramic and Silicate Institute, Haifa, Israel*

Abstract: In this study we fabricated, for the first time, magnesium gallate (MgGa$_2$O$_4$, a partially inverted spinel) transparent ceramics, both undoped and doped with 1 at% Ni. The specimens were derived from in-house prepared powder, with a crystallite size of ~10 nm (by wet chemistry) and densified by pulsed electric current sintering (PECS; peak temperature 950 ℃ for 90 min). Densification levels of 99.84% and 99.52% of theoretical density were attained for doped and undoped materials, respectively. Doping with Ni was seen to marginally improve the densification level. Quite transparent specimens were produced: the best showing transmission of ~89% of the theoretical level (thickness t = 0.85 mm). The absorption spectra revealed that the dopant was accumulated as Ni^{2+} in the octahedral sites of the lattice, as occurs in single-crystal specimens. After excitation at 980 nm, the doped disks exhibited a wide fluorescence band centered at 1264 nm.

Keywords: magnesium gallate (MgGa$_2$O$_4$); spinel; transparent ceramics; pulsed electric current sintering (PECS)

1 Introduction

Magnesium gallate (MgGa$_2$O$_4$) is a stiff, refractory (melting point ~1930 ℃), double oxide, with an intermediate band gap value (~4.9 eV) that makes it possible to produce both insulator and conductive variants, as well as being resistant to decomposition until close to its melting point [1]. In its opaque state, it has various applications, including electronics, energy production, and spintronics [1,2], but the most interesting applications are those that exploit the fact that transparency (in the single crystal state) can be coupled with n-type electronic conductivity [1,3]. For instance, photodetectors, gas sensors, transparent electrodes, solid-state phosphors, waveguides, LEDs,

or lasing ion hosts (operation at < 100 K) may be derived from this material [3–7]. Moreover, owing primarily to the partially inverted character of its cubic lattice, MgGa$_2$O$_4$ is a useful host for transition metal (TM) cation dopant spectroscopy (see Section 2).

For applications and spectral studies on transparent MgGa$_2$O$_4$, only single crystals are available currently, to the best of our knowledge. It is worth noting that because the material is cubic and resistant to decomposition, it can be obtained easily, in principle, in polycrystalline (ceramic) form by, for example, powder compact sintering. The incentive to use such an option is that this type of fabrication is significantly simpler and less costly than single crystal growing [8].

In the research described here, our main objective was to establish an MgGa$_2$O$_4$ ceramic fabrication procedure, based on pulsed electric current sintering (PECS), that would allow us to obtain transparent parts.

* Corresponding author.
E-mail: wuy@alfred.edu

PECS was selected because, despite being a relatively new procedure, it has been shown to be an efficient technique for obtaining transparent ceramics compared with other firing approaches [9–11].

Because of the relevance (noted above) for TM cation spectroscopy of the material, we also investigated the spectral (optical) behavior of the Ni-doped transparent magnesium gallate ceramics. Nickel was chosen as the first TM dopant because lots of data exist for $MgGa_2O_4$ doped with Ni single crystals, allowing for comparison [12,13]. Its potential use as a lasing ion (at temperatures < 100 K) increased our interest in this dopant [12–14].

2   Differences in the configuration of $MgGa_2O_4$ and $MgAl_2O_4$ lattices

To clarify why magnesium gallate is an interesting host for TM spectral studies, it is worth reviewing the essential aspects of its lattice structure and comparing it with that of Mg, Al spinel.

$MgGa_2O_4$, like $MgAl_2O_4$, belongs to the AB_2O_4 family of double oxides called spinels (where A and B can be fulfilled by various cations with oxidation states between 2+ and 4+; non-oxide spinels also exist). "Spinel" is both the name of this material and of the lattice type, the archetype of the family being $MgAl_2O_4$. Thus, all family members have a lattice similar to that of Mg, Al spinel. The symmetry of the lattice is indicated, usually, to correspond to the $Fd3m$ space group, an approximation satisfactory in most cases, of the actual O_h^7 ($F_{1/d}^4\bar{3}_{2/m}$) No. 227 space group. A detailed description of this lattice is given in Ref. [15].

An important feature of this lattice type is the relative ease of inversion. Recall that inversion means (in this context) that compared with the ideal spinel lattice, where A cations normally lie on tetrahedral sites, A cations can reside on octahedral sites, and vice versa for B cations. The process is quantified by a parameter i, which is equal to the number of A cations residing on octahedral sites. Therefore, a more complete description of a spinel composition also indicates the value of i, taking the form of Eq. (1):

$$(A_{1-i}B_i)^{IV}[A_iB_{2-i}]^{VI}O_4 \qquad (1)$$

For a normal spinel (e.g., $MgAl_2O_4$), $i = 0$, where A cations occupy 8 out of 64 tetrahedral sites, and B cations occupy half (16) of the octahedral sites. For a completely inverted spinel (e.g., $MgIn_2O_4$), $i = 1$,

where B cations occupy 8 out of the 64 tetrahedral sites, and both A and B cations share half of the octahedral sites (8 each, 16 in total); such a lattice corresponds, in fact, to a $B(AB)O_4$ formula. For the ideal $MgGa_2O_4$, i is in the range from 2/3 to 1; thus, it is a partially inverted spinel. Thermodynamic calculations show that the enthalpic component of the spinel-type lattice free energy depends more on i than the entropic component. The enthalpy depends mostly on the energy associated with the electrostatic fields operating within the lattice [16]. The situation changes only at temperatures close to the melting point. In that region, entropy controls lattice energy and all spinels tend to assume an i-value corresponding to total randomness ($i = 2/3$). One consequence of enthalpy dominance at low to moderate temperatures is the counterintuitive but practically verified rule that the larger the cation (of A or B type), the more it is likely to seek tetrahedral sites (the rule holds, for example, in the series Al < Ga < In). The $MgAl_2O_4$ and $MgGa_2O_4$ lattices are schematized in Fig. 1 [17].

From the above, it is apparent that an incoming TM cation will find 2+ native cations on the tetrahedral sites of $MgAl_2O_4$ and mostly 3+ cations in the case of $MgGa_2O_4$. This may lead, in certain cases, to the accumulation of a given TM cation on different site types in Al versus Ga spinels. As a result, their optical spectra may differ significantly. This is the main reason, as noted at the beginning of the introductory section, why it is necessary to compare the spectra of TM cations when they have either Ga or Al spinels as hosts. The gathered data may shed light on the way the TM cation and native cation exchange processes occur (a basic issue in materials science).
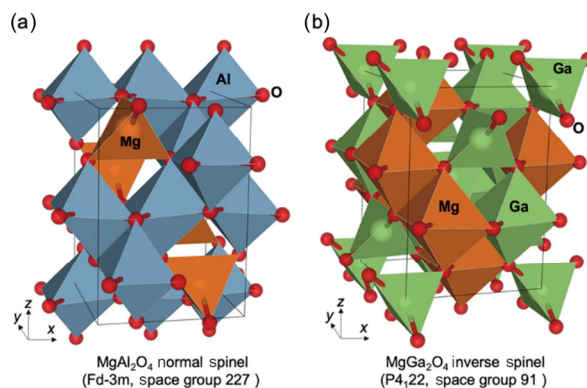

Fig. 1   Normal and inverse spinel structures: (a) $MgAl_2O_4$ and (b) $MgGa_2O_4$. Reproduced with permission from Ref. [17]; this is a U.S. government work and not under copyright protection in the U.S.; foreign copyright protection may apply 2020.

3   Experimental

3. 1   Ceramic powder synthesis

$Ga(NO_3)_3 \cdot xH_2O$ (99.9%, Alfa Aesar, USA), $Ni(NO_3)_2 \cdot 6H_2O$ (99.999%, Sigma-Aldrich, USA), and $Mg(NO_3)_2 \cdot 6H_2O$ (99.999%, Sigma-Aldrich, USA) were used as starting materials. The crystallization water of these hydrated nitrate salts was determined by a calcination process at 1000 ℃ for 5 h. $MgGa_2O_4$ and Ni^{2+}-doped $MgGa_2O_4$ ceramic powder was prepared by a nitrate pyrolysis method. The nitrate hydrate salts were dissolved in deionized water in amounts according to the stoichiometry ratio. The nitrate solution was then stirred and heated on a hot plate at approximately 300 ℃ until the transparent solution turned into a gel. The nitrate gel was transferred to a furnace and thermally treated at 1000 ℃ for 1 h. The thermal treatment converted the gel into a xerogel, leading to crystallization of the latter to $MgGa_2O_4$. Finally, the obtained ceramic powder was ball milled in anhydrous alcohol for up to 24 h.

3. 2   MgGa₂O₄ and Ni-doped MgGa₂O₄ ceramic fabrication

After drying, the ball milled powder was further deagglomerated before inserted in the die using an agate mortar and pestle. For sintering, a PECS machine (HP D 25, FCT Systeme GmbH, Germany) was used. The ceramic powder was loaded into a graphite tool with inner molybdenum foil and outer graphite foil, to isolate the graphite tool from the loaded ceramic powder. Molybdenum foil has been reported to suppress carbon contamination [18]. BN powder was also added as a buffer layer, to absorb mechanical or thermal shock and reduce any potential carbon diffusion to the ceramic powder. It can also reduce gallium decomposition for the sintering of $MgGa_2O_4$.

A typical sintering schedule, including the profile of the applied force and temperature variation, is given in Fig. 2, and a two-step sintering profile was applied. Two-step sintering can expedite the pore closure process because it provides a better particle size distribution (the initial size distribution is wide) at the end of the first stage of sintering due to a pre-coarsening process [19,20]. The measured parameters include the actual force (set force-profile is also shown), the measured tool surface temperature (pyro B; maximal set temperature is also shown), the piston moving speed, and the relative piston position. The ceramic powder was heated from 450 to 850 ℃, at a ramping rate of 50 ℃/min with a pressure increasing from 3 kN (10 MPa) to 14 kN (48 MPa). The sample was then held at 850 ℃ for 5 min. Then, the sintering temperature was increased to 950 ℃, again at 50 ℃/min, and the pressure was raised to 27 kN (93 MPa). The temperature was maintained at 950 ℃ for dwell time of 1 h and 30 min. To avoid cracking caused by mechanical and thermal shock, the pressure was reduced, after sintering, to a minimum of 3 kN in 15 min while holding the temperature at 950 ℃. Finally, the firing process was terminated by shutting power at 950 ℃ and cooling to room temperature naturally. The piston moved significantly in the three regions
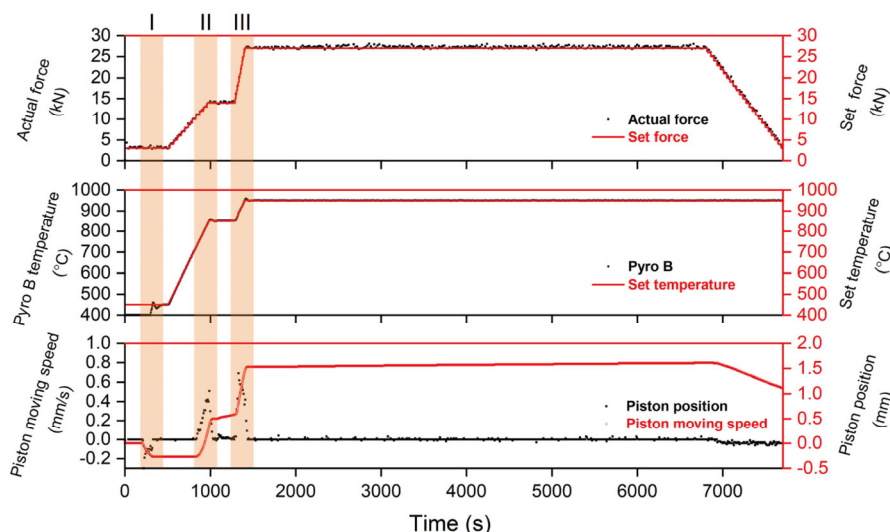

Fig. 2   Typical PECS profile of force and temperature for transparent $MgGa_2O_4$ ceramic fabrication with real-time measured parameters including actual force, pyro B temperature, piston moving speed, and relative piston position.

shown in Fig. 1, noted as I, II, and III. In stage I, the piston moved in a negative direction due to carbon expansion during the heating process. In stages II and III, the piston moved in a positive direction, indicating that the densification process was linked to heating- and pressure-related deformation. Maximum densification was achieved within 2 min after reaching 950 ℃.

3. 3   Characterization

The crystalline phase identification of the synthesized ceramic powder and PECS-treated ceramics was performed by X-ray diffraction (XRD) on a D2 Phaser (Bruker, Germany) diffractometer, using Cu Kα radiation. The lattice constant of ceramics was determined after Rietveld refinement of the raw data for theoretical density calculation. Densities were measured based on Archimedes' principle. The morphology of synthesized ceramic powder and microstructure of sintered ceramics was studied using FEI Quanta 200F scanning electron microscopy (SEM). Thermal etching was applied to the dense ceramic specimens for SEM, at 1300 ℃ for 30 min. Sintered ceramics were mirror polished on both sides for optical characterization (thickness $t = 0.85$ mm). Transmittance and absorption spectra of transparent ceramics were measured by using a UV/VIS/NIR spectrophotometer (Evolution 220; Thermo Scientific, USA). Raman spectra of transparent $MgGa_2O_4$ ceramics were obtained by using a Raman spectrometer (ALPHA300 RA, WITec, Germany) with a 480 nm laser. The optical quality of the fabricated transparent ceramics was evaluated by optical photo, and Schlieren images were taken, respectively, using a cell phone and a homemade Schlieren imaging system. Photoluminescence spectra were measured by Jobin Yvon Fluorolog-3 spectro-fluorometer system (Horiba, Kyoto, Japan).

4   Results and discussion

4. 1   Phase composition and effect of particle size on densification

To identify crystalline phase of both as-synthesized $MgGa_2O_4$ and 1% Ni-doped powder, the powder XRD patterns (see Fig. 3) were measured, which fit well with ICDD Powder Diffraction File (PDF) cards 01- 087-1178 and 04-007-2717. This result showed that both materials exhibited a single phase with a spinel- type structure. The two PDF cards refer to spinel lattices differing in the level of inversion; however, the XRD patterns they carry are similar. In our discussion, they will be treated simply as spinel-type structures. The crystallite size, L_s, of the ceramic powder could be determined using the Scherrer formula: $L_s = 0.92\lambda/\beta_s\cos\theta_B$, where λ is the wavelength of XRD (Cu Kα radiation with $\lambda = 0.154$ nm), β_s is the peak full width at half maximum (FWHM) of the diffraction peak, and θ_B is the Bragg angle. The crystallite sizes of $MgGa_2O_4$ and 1% $Ni:MgGa_2O_4$ powder were calculated to be 10.8 and 11.2 nm, respectively.

Agglomeration is a commonly observed situation in ceramic powder synthesized by wet chemistry, and those prepared using the nitrate pyrolysis method are no exception [21]. Ball milling is a widely used method to effectively deagglomerate ceramic powder [22]. The morphology evolution of $MgGa_2O_4$ ceramic powder, with the increae of ball milling time, is illustrated in the SEM images of Figs. 4(a)–4(e). Strong agglomeration of $MgGa_2O_4$ powder is clearly seen in Fig. 4(a) and confirmed by the crystalline sizes calculated from the XRD patterns. Figure 4(b) shows that large agglomerates of $MgGa_2O_4$ powder were disintegrated by the ball milling process. Extending the ball milling time from 4 to 12 h did not greatly
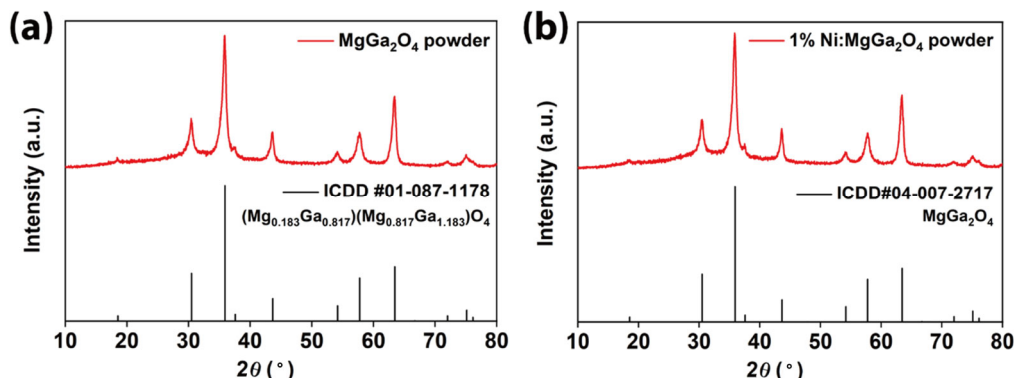

Fig. 3   XRD patterns of synthesized (a) $MgGa_2O_4$ and (b) 1% $Ni:MgGa_2O_4$ ceramic powder.

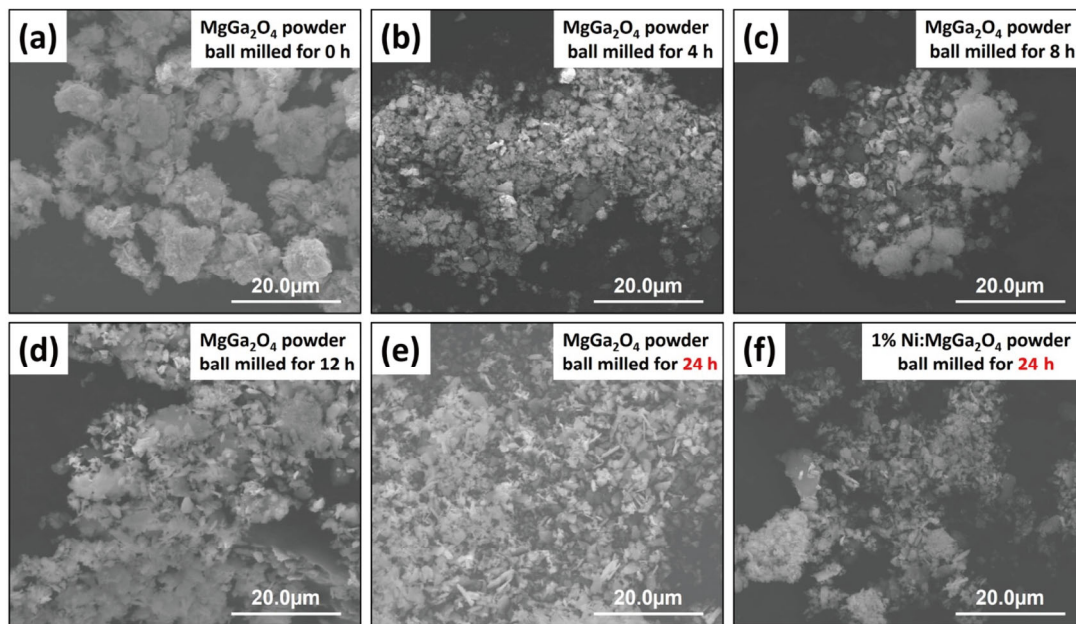**Fig. 4** SEM micromorphology images of MgGa$_2$O$_4$ ceramic powder ball milled for (a) 0 h, (b) 4 h, (c) 8 h, (d) 12 h, and (e) 24 h, and (f) 1% Ni:MgGa$_2$O$_4$ ceramic powder ball milled for 24 h.
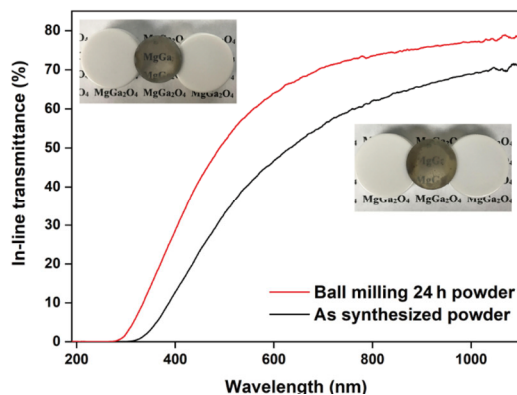

Fig. 5 Transmittance of sintered transparent MgGa$_2$O$_4$ ceramics derived by PECS from as-synthesized and 24-h ball milled ceramic powder ($t = 0.85$ mm).

improve deagglomeration. However, after 24 h of ball milling, a significantly more uniform particle size distribution was achieved in both MgGa$_2$O$_4$ and Ni-doped material, as seen in Figs. 4(e) and 4(f), respectively.

Both as-synthesized and 24-h ball milled MgGa$_2$O$_4$ ceramic powder was sintered into transparent ceramics by PECS using the same profile as shown in Fig. 2. The polished transparent ceramics and their transmittance are plotted in Fig. 5. From the inserted sample images, it is clearly seen that MgGa$_2$O$_4$ as-sintered ceramic powder, derived from unmilled powder, is hazy, with many black dots as scattering centers. The number of these defects was effectively reduced by using 24-h ball milled MgGa$_2$O$_4$ ceramic powder.

Milling of the powder improved transmittance by about 10%, as can be seen in Fig. 5. Thus, ball milling for 24 h in anhydrous alcohol was applied to the Ni:MgGa$_2$O$_4$ ceramic powder.

With 24-h ball milled starting ceramic powder, dense and transparent MgGa$_2$O$_4$ and 1% Ni:MgGa$_2$O$_4$ bulk parts were successfully fabricated by PECS. Phase identification of the dense specimens was achieved based on XRD patterns and Rietveld refinement, as shown in Fig. 6. The measured XRD patterns were almost identical to those generated by the raw ceramic powder, indicating the same spinel-type crystalline structure. Based on the results of Rietveld refinement, lattice constants and theoretical densities were calculated and are summarized in Table 1. Relative densities of 99.52%±0.21% and 99.84%± 0.14% were obtained for MgGa$_2$O$_4$ and 1% Ni:MgGa$_2$O$_4$ ceramics, respectively (XRD-derived density was taken as the theoretical density). Considering the level of uncertainty of the Archimedes technique, the determined values of bulk density cannot be used to accurately predict the level of optical transparency attained [8]. However, the values show that the specimens attained a level of densification at which they may show transparency. Figure 5 indicates that a transmission level of ~89% of the theoretical level (~80% in absolute units) was attained for most of the spectral region of interest.

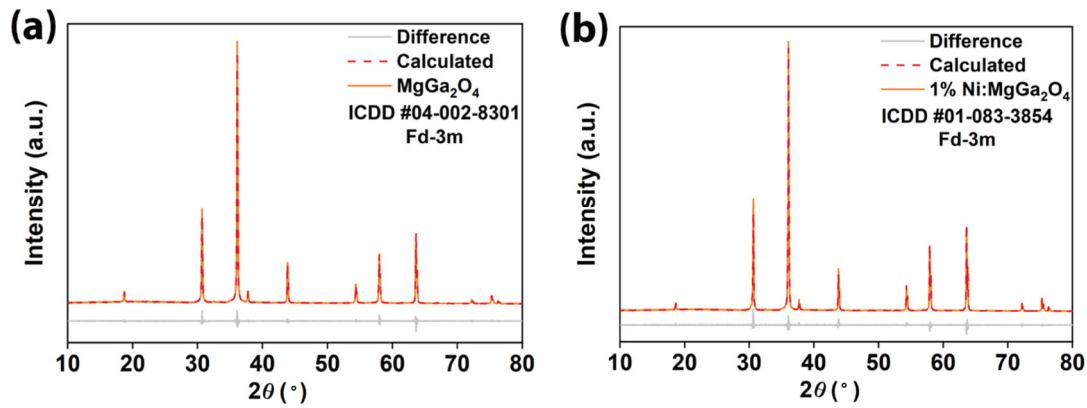**Fig. 6** XRD patterns and Rietveld refinement of fabricated (a) $MgGa_2O_4$ and (b) 1% $Ni:MgGa_2O_4$ transparent ceramics.

Table 1 Unit cell constant calculated by Rietveld refinement from XRD data, calculated theoretical density (from XRD data), measured density, and calculated relative density of $MgGa_2O_4$ and 1% $Ni:MgGa_2O_4$ ceramics

Sample	$a = b = c$ (Å)	$\alpha = \beta = \gamma$ (°)	V (Å^3)	Theoretical density (g/cm^3)	Measured density (g/cm^3)	Relative density
$MgGa_2O_4$	8.2885(2)	90	569.41(8)	5.3136	5.288 ± 0.011	99.52% ± 0.21%
1% $Ni:MgGa_2O_4$	8.2779(4)	90	567.23(9)	5.3414	5.333 ± 0.018	99.84% ± 0.34%

4. 2 Raman spectroscopy

Raman measurements were made in order to estimate the level of carbon penetration during sintering and confirm the presence of inversion in the lattice.

The measured overall Raman spectra of the ceramic specimens are shown in Fig. 7(a), which also includes the spectra of a graphite die and a graphite spacer. From the enlarged view (see Fig. 7(b)) of the domain containing carbon-generated signals, it can be seen that the ceramics before and after annealing did not exhibit the D and G bands typical of carbon [18,23]. This indicates that diffusion of carbon into the sintering specimen was slowed by using Mo foil, so that its content was significantly reduced, although not all carbon was eliminated. In the absence of the metal foil, the amount of carbon entering specimens subjected to

PECS or simple hot-pressing is sufficient to generate Raman signals [24]. This reduction was very helpful because the amount of carbon entering, which cannot be completely prevented, was nonetheless sufficiently low to allow its elimination by low-temperature air annealing subsequent to sintering. High-temperature annealing of specimens subjected to pressure-assisted sintering carries a risk of re-enlargement of the nano-sized pores produced during sintering [25].

The Raman shift domain, which includes the signals caused by host-lattice vibrations (at 752.2, 640.1, 526.7, 370.9, and 204.2 cm^{-1}), is shown in Fig. 7(c). The measured Raman spectra matched well with those reported in the literature for $MgGa_2O_4$ ceramics and crystals [26–28]. From group theory analysis, the vibrational modes of a spinel ($Fd3m$) at $k = 0$, in a
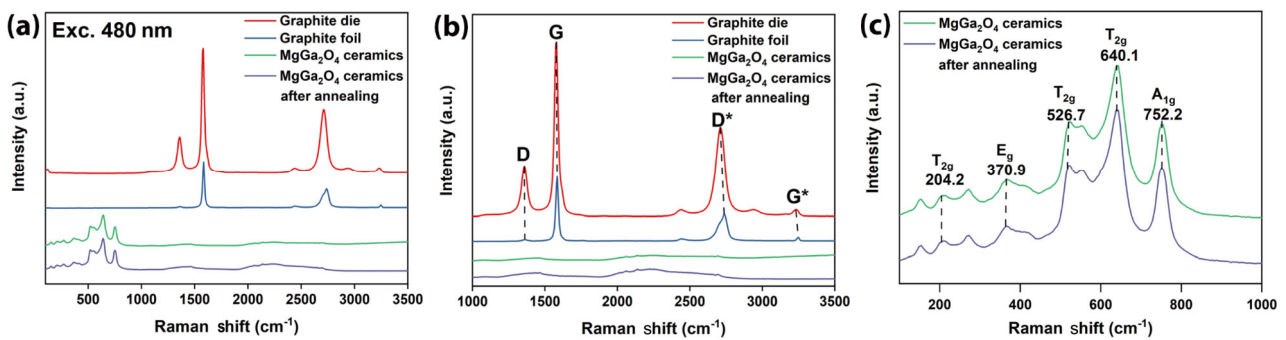

Fig. 7 (a) Raman spectra of graphite die, graphite foil, and $MgGa_2O_4$ ceramics before and after annealing, (b) enlarged Raman spectra of graphite, and (c) enlarged Raman spectra of $MgGa_2O_4$ spinel structure.

primitive cell, are $A_{1g}(R) + E_g(R) + 3T_{2g}(R) + 4T_{1u}(IR) + T_{1g} + 2A_{2u} + 2E_u + 2T_{2u}$ [29,30]. Only five modes $(A_{1g}(R) + E_g(R) + 3T_{2g}(R))$ were Raman active [30]. The observed band energies (see Fig. 7(c), which contain the signals generated by the lattice vibrations), were assigned to those Raman-active vibrational modes, namely, A_{1g}, $T_{2g}(3)$, $T_{2g}(2)$, E_g, $T_{2g}(1)$ [31].

The asymmetric peaks can be deconvoluted into doublets (as observable even by visual inspection), indicating that indeed the host is partially inverted. The Raman spectrum is sensitive to local host geometry. In normal spinels, all the octahedral sites are occupied by the B type cations. In partially (like here) or fully inverted spinels, the octahedral sites are occupied by two types of cations, here Mg^{2+} and Ga^{3+}. The geometry of the sites that include Ga versus Mg is slightly different, generating the observed band split [32]; in fully inverted hosts, the splitting is more accentuated.

4. 3   Microstructure examination

Some aspects of the microstructure such as densification level, grain size, and morphology were studied by using SEM.

The SEM micromorphology images of polished and thermal etched surfaces, fracture surfaces, and corresponding average grain size distributions are illustrated in Fig. 8 to evaluate the quality of the sintered ceramics. As can be seen in Figs. 8(a) and 8(d), both ceramics exhibited a sub-micron grain size with relatively uniform distribution. The average grain size, measured from fracture images of Figs. 8(b) and 8(e), matched well with the values obtained from the polished and thermal etched surfaces; this demonstrates isotropic grain growth. The average grain sizes, derived from Figs. 8(c) and 8(f), were 0.53 and 0.44 μm for transparent $MgGa_2O_4$ and 1% $Ni:MgGa_2O_4$ ceramics, respectively; the average grain size of undoped $MgGa_2O_4$ was slightly larger than that of 1% $Ni:MgGa_2O_4$. This suggested that Ni ion dopants could partially slow grain growth during PECS, leading to a more uniform grain size distribution for the 1% Ni-doped specimens, as shown in Fig. 8(f), together with a slightly higher fired bulk density level.

4. 4   Optical absorption and emission spectroscopy

4.4.1   General transmission and color

The transmission (near UV–VIS–NIR region) of sintered and annealed specimens of both undoped and Ni-doped disks is shown in Fig. 9.

As the insets of Fig. 9 illustrate, the as-sintered ceramics exhibited a dark-brown coloration. To remove this coloration, a post-sintering and low-temperature air-annealing treatment (900 ℃ for 15 h) was
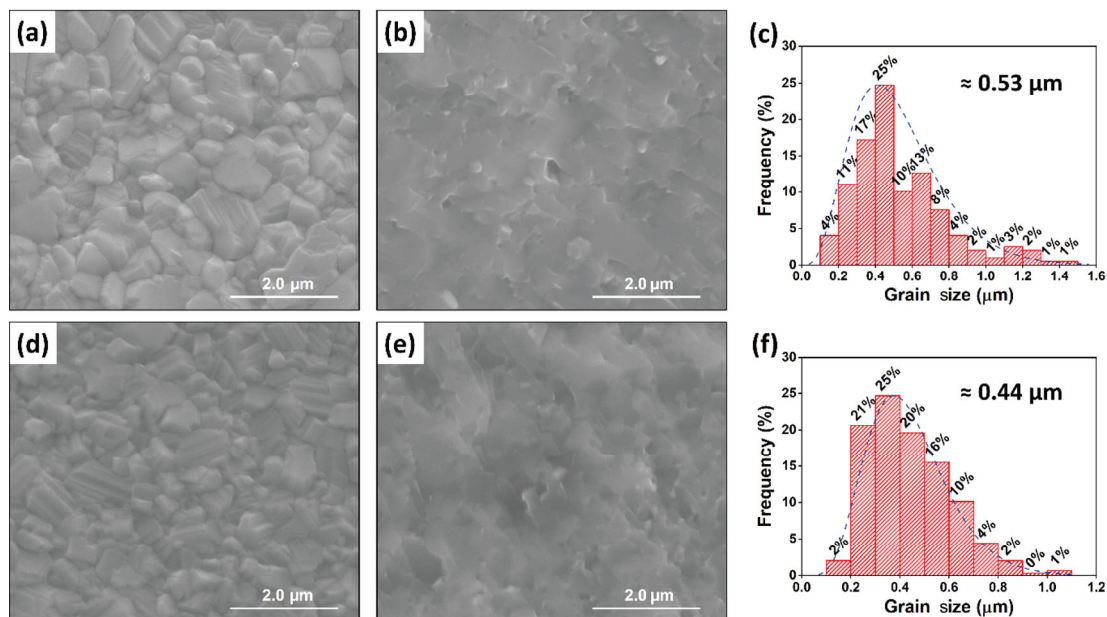

Fig. 8 SEM micromorphology images of (a) polished and thermal etched surface and (b) fracture surface, and (c) grain size distribution of $MgGa_2O_4$ transparent ceramics; and SEM micromorphology images of (d) polished and thermal etched surface and (e) fracture surface, and (f) grain size distribution of 1% $Ni:MgGa_2O_4$ transparent ceramics.
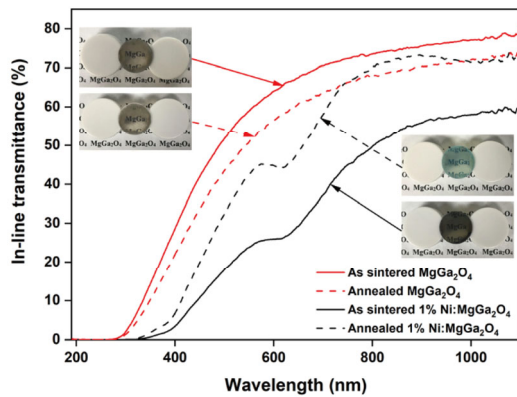
Fig. 9 Transmittance of pure and Ni-doped transparent MgGa$_2$O$_4$ ceramics before and after annealing at 900 ℃ for 15 h (t = 0.85 mm).

necessary. Annealing led to a drastic reduction of the color intensity of the undoped specimens but also reduced the average transmission level by about 5%. In contrast, air annealing of the Ni-doped MgGa$_2$O$_4$ ceramics replaced the intense brownish tint with a lighter and bluish-green color, similar to that of a single crystal grown by the floating zone method [13]. Annealing of the Ni-doped MgGa$_2$O$_4$ ceramics also uncovered a band in the near infrared region, not seen in the as-sintered state; this band was due to the transition to $^3T_{2g}(^3F)$ energy level (see below) [12]. The highest transmittance of pure and Ni-doped MgGa$_2$O$_4$ ceramics, after annealing, was 73.3% (at ~1.2 µm) and 72.6% (at ~0.85 µm), respectively.

The changes in transmittance before and after annealing can be rationalized by considering two simultaneous effects of carbon on incoming light; it absorbs light (uniformly at the various frequencies of the visible domain so that gray to black hues are produced) but also affects the average value of the refraction index (reducing the difference between this average and that of the pores). The latter reduces the intensity of light loss due to the scattering of pores. Although both the undoped and Ni-doped specimens retained low amounts of porosity, the former retained more than the latter. Therefore, for undoped specimens, the increase of the difference between the refraction index of the solid and gas led to a greater loss than the improvement brought by the elimination of carbon; the overall effect was a reduction in transmission. For the less porous Ni-doped disks, the elimination of carbon absorption was dominant, so that overall, the carbon-free specimens had improved transmission.

The transmission of the annealed specimens was

sufficiently high to allow the recording of Schlieren-type images (see Figs. 10(c) and 10(d)). This type of image is taken after illuminating at an angle different from 90°; Schlieren imaging takes variation in the refractive index into account and is therefore a good method to evaluate inhomogeneities and volume defects inside transparent ceramics [33]. Unlike SEM surface observation, Schlieren imaging also collects information on defects located inside the specimen. Thus, it reveals the defects present in the whole measured volume, instead of only the surface defects shown by SEM observation. It supplements the information on defects provided by SEM, especially macroscopic ones such as cracks. In our case, these images showed an orange-peel texture caused by pores and cracks. It can be seen that such defects extend inside the specimen although they are more numerous toward the surface. The Schlieren images were taken with a homemade Schlieren imaging system, making it hard to determine the measurement scale. However, both images were taken with the same set-up. Thus, we can make a qualitative comparison of defects in doped and undoped specimens using these images. It can be seen that the MgGa$_2$O$_4$ ceramics exhibited a much larger number of pores and cracks than the Ni-doped specimens. The pores and cracks likely explain the decreased in-line transmittance of MgGa$_2$O$_4$ ceramics after annealing; residual pores are an important and common issue for most PECS-sintered transparent ceramics [34]. A comparison of Figs. 10(c) and 10(d) strengthens the fact, shown in Fig. 5, that is, the higher densification level attained by the Ni-doped specimens.
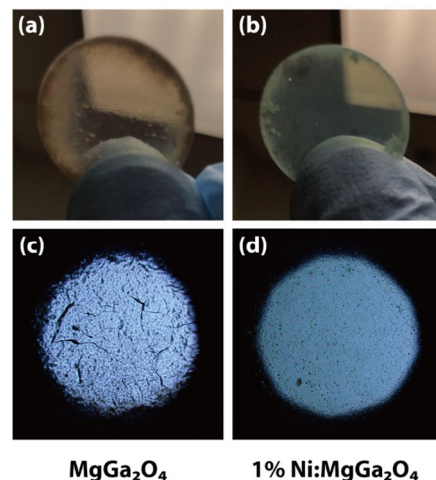

Fig. 10 Optical images of (a) MgGa$_2$O$_4$ and (b) 1% Ni:MgGa$_2$O$_4$, and Schlieren images of (c) MgGa$_2$O$_4$ and (d) 1% Ni:MgGa$_2$O$_4$.

In this context, it is worth underlining again that very small differences in residual pore content have a significant effect on transmission values [8].

The overall transmission level of the specimens is adequate for spectral measurements and some applications. For more demanding applications, it is necessary to further improve it (by at least 4%–5%), especially at wavelengths lower than 600 nm.

4.4.2 Interpretation of absorption spectra of Ni-doped specimens

The transmittance curve of the PECS-treated doped ceramics shows three significant absorption peaks. When absorbance is shown as a function of wavelength (see Fig. 11), the data reveal the presence of some very weak additional signals. Nickel in $MgGa_2O_4$ transparent ceramics is expected to assume the Ni^{2+} state (a $3d^8$ electronic configuration) because Ni^{1+} has an ionic radius too large to allow easy exchange with native cations and a crystal field stabilization energy (CFSE) much lower than that of Ni^{2+}. Ni^{3+} also has a lower CFSE than Ni^{2+} (1.2 × 10Dq vs. 0.8 × 10Dq for Ni^{3+}; 10Dq = ligand field strength), and the ionization energy necessary to increase the oxidation state from 2+ to 3+ is large. For Ni^{2+} cations, coordination numbers of six and four are, in principle, possible. The former is more likely because it has a CFSE 60% higher than the latter [13], but tetrahedral Ni^{2+} is also reported in transparent oxide hosts [35]. The general profile of the spectra, recorded here and shown in Fig. 11,
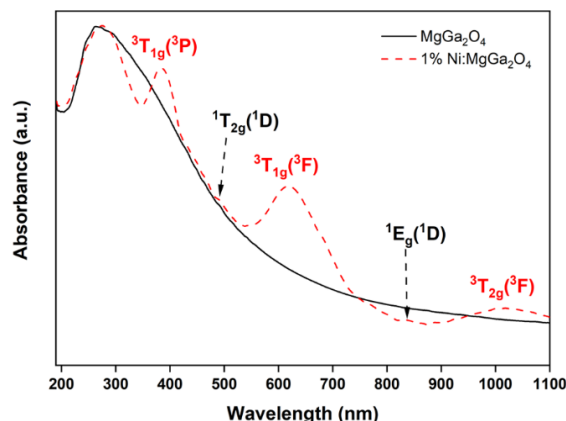

Fig. 11 Absorption spectra of $MgGa_2O_4$ and 1% $Ni:MgGa_2O_4$.

suggests Ni^{2+} in an octahedral site as the cause of the absorption bands.

For a clearer band assignment, the recorded spectra were interpreted using the Tanabe–Sugano diagram pertinent for a d^8 configuration ion in an octahedral ligand field. The diagram is shown in Fig. 12. The observed spectrum could be fitted to the diagram taking the values $Dq = 982.3$ cm^{-1} and $B = 825.3$ cm^{-1}; this corresponds to a value of 11.9 for the 10Dq/B ratio. As a result, the strong bands of Ni-doped $MgGa_2O_4$ ceramics (at 1018, 618, and 383 nm) could be assigned to the spin-allowed transitions from the ground state to the $^3T_{2g}(^3F)$, $^3T_{1g}(^3F)$, and $^3T_{1g}(^3P)$ excited levels, respectively. The lowest energy band became visible only after the annealing treatment. In addition to the three spin-allowed transitions of Ni^{2+}, from an $^3A_{2g}$
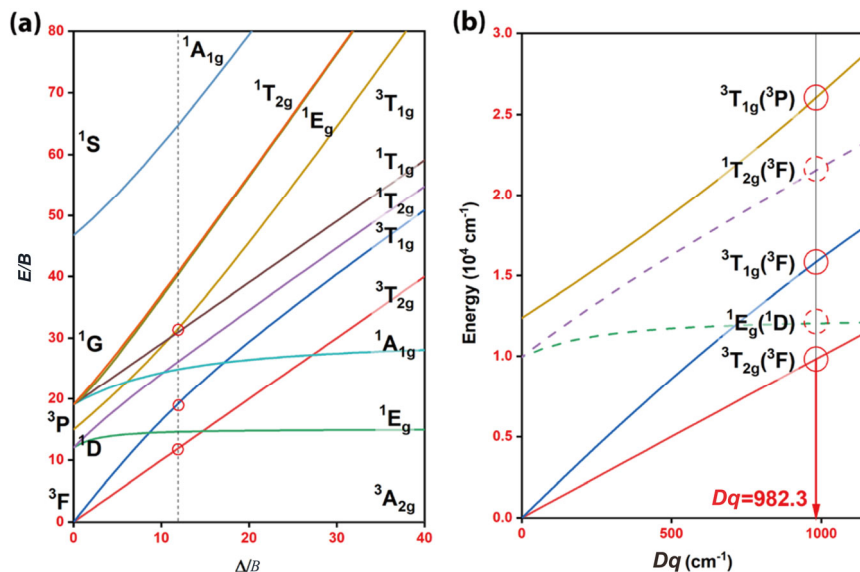

Fig. 12 (a) Tanabe–Sugano diagram of d^8 octahedral (O_h) (for $Dq = 982.3$ cm^{-1}, $B = 825.3$ cm^{-1}, and $C = 2918.7$ cm^{-1}); the vertical dashed line marks the 1% $Ni:MgGa_2O_4$ transparent ceramics. (b) Enlarged energy diagram of octahedral Ni^{2+} doped in $MgGa_2O_4$ transparent ceramics.

Table 1   Energy levels of Ni^{2+} in MgGa$_2$O$_4$ transparent ceramics from measurement and theoretical prediction

Energy level	Measured (cm^{-1})	Theoretical (cm^{-1})
$^3T_{2g}(^3F)$	9823.18	9821.38
$^1E_{1g}(^1D)$	12048.19	12058.01
$^3T_{1g}(^3F)$	16181.23	15854.51
$^1T_{2g}(^3F)$	20618.56	21623.54
$^3T_{1g}(^3P)$	26109.66	26080.30

Fig. 13   Tauc plot of MgGa$_2$O$_4$ and 1% Ni:MgGa$_2$O$_4$ transparent ceramics.

ground state to $^3T_{1g}(^3P)$, $^3T_{1g}(^3F)$, and $^3T_{2g}(^3F)$ observed at 383, 618, and 1018 nm, another two spin-forbidden transitions, from an $^3A_{2g}$ ground state to $^1T_{2g}(^3P)$ and $^1E_{1g}(^1D)$, were observed at 485 and 830 nm respectively (see Fig. 11). These five energy levels are summarized in Table 2. All bands of the absorption spectrum in Fig. 11 could be assigned to octahedral Ni^{2+} without doubt. This demonstrates that no Ni^{2+} exists in tetrahedral sites. Similar optical absorption was observed in Ni-doped MgGa$_2$O$_4$ single crystal [13]. Thus, both the single crystal and ceramic Ni-doped specimens confirm the absence of tetrahedrally coordinated Ni^{2+}. This is reasonable considering that NiGa$_2$O$_4$ is reported to exhibit inversion levels of up to 92% [12,13,36]; actual inversion levels depend on the thermal history of the specimens.

4.4.3   Determination of the band gap energy

The optical bandgap is evaluated from absorption in Fig. 11 based on a Tauc relation:

$$\alpha h v \approx (h v - E_g^{opt})^n \qquad (2)$$

where α is the absorption coefficient, h is the Planck constant, v is the photon's frequency, and E_g^{opt} is the optical band gap. The exponent n can be 1/2 and 2, which correspond to both direct and indirect allowed transition band gaps, respectively [37]. The optical band gap is given by x-axis intersection point of extrapolation on the linear portion of the Tauc plot based on absorption. The Tauc plots of MgGa$_2$O$_4$ and 1% Ni:MgGa$_2$O$_4$ ceramics are plotted in Fig. 13. It allowed the determination of direct allowed transition band gap, by extrapolation, of the optical band gaps of MgGa$_2$O$_4$ and 1% Ni:MgGa$_2$O$_4$ ceramics, being 4.75 and 4.43 eV, respectively.

4.4.4   Photoluminescence

The photoluminescence spectrum of 1% Ni:MgGa$_2$O$_4$ transparent ceramics was obtained with a 980 nm laser beam, as shown in Fig. 14. The broad emission
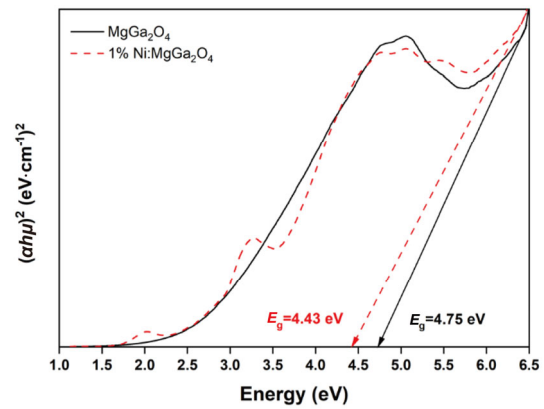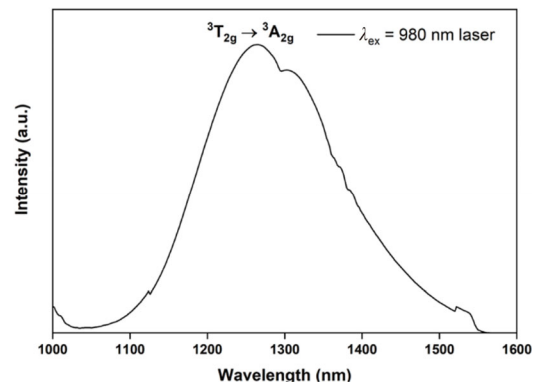

Fig. 14   Photoluminescence emission spectrum of 1% Ni:MgGa$_2$O$_4$ transparent ceramics excited at 980 nm.

(because of the strong vibronic character of the transition generating the optical signal), in a range from 1000 to 1600 nm, centered at 1264 nm. It matched well with the photoluminescence emission seen for the 1% Ni:MgGa$_2$O$_4$ single crystal, as reported by Suzuki *et al.* [13] and others, for various Ni-doped spinel-type hosts such as ZnAl$_2$O$_4$, ZnGa$_2$O$_4$, ZnCr$_2$O$_4$, and MgAl$_2$O$_4$ [38,39]. The Tanabe diagram suggests the $^3T_{2g}(^3F)$ to $^3A_{2g}$ transition (the only one giving a reasonable Stokes shift value) as the cause of the fluorescence band recorded by us and other authors. The absorption and emission spectroscopy data suggest that Ni^{2+} has a similar optical behavior in single crystals and ceramics of the MgGa$_2$O$_4$ type.

5   Conclusions

In this study, quite transparent (~89% of theoretical value) MgGa$_2$O$_4$ and Ni^{2+}-doped MgGa$_2$O$_4$ spinel ceramics were fabricated using powder synthesized in

house and a simple nitrate pyrolysis method. The pure $MgGa_2O_4$ and Ni^{2+}-doped $MgGa_2O_4$ spinel ceramics could be sintered to nearly full densification (relative densities of 99.52% and 99.84%) by low-temperature PECS at 950 ℃ for 1 h and 30 min; doping slightly increased the densification level. The average grain sizes were 0.53 and 0.44 μm, respectively. The measured transmittance of pure and Ni-doped $MgGa_2O_4$ ceramics, after annealing, was 73.3% (at 1.2 μm) and 72.6% (at 0.85 μm). The band gaps were 4.75 and 4.43 eV, respectively. The Ni^{2+}:$MgGa_2O_4$ transparent ceramics exhibited a broad band emission in the range from 1000 to 1600 nm, centered at 1264 nm, when excited by a 980 nm laser.

Acknowledgements

References

[1]   Hirschle C, Schreuer J, Galazka Z. Interplay of cation ordering and thermoelastic properties of spinel structure $MgGa_2O_4$. *J Appl Phys* 2018, **124**: 065111.

[2]   Sukegawa H, Kato Y, Belmoubarik M, *et al.* $MgGa_2O_4$ spinel barrier for magnetic tunnel junctions: Coherent tunneling and low barrier height. *Appl Phys Lett* 2017, **110**: 122404.

[3]   Galazka Z, Klimm D, Irmscher K, *et al.* $MgGa_2O_4$ as a new wide bandgap transparent semiconducting oxide: Growth and properties of bulk single crystals. *Phys Status Solidi A* 2015, **212**: 1455–1460.

[4]   Pedro SS, Silva M, López A, *et al.* Structural and photoluminescent properties of the $MgGa_2O_4$:Co^{2+} ceramic compound revisited after two decades. *J Adv Ceram* 2015, **4**: 267–271.

[5]   Basavaraju N, Sharma S, Bessière A, *et al.* Red persistent luminescence in $MgGa_2O_4$:Cr^{3+}; a new phosphor for *in vivo* imaging. *J Phys D: Appl Phys* 2013, **46**: 375401.

[6]   Li Y, Niu P, Hu L, *et al.* Monochromatic blue-green and red emission of rare-earth ions in $MgGa_2O_4$ spinel. *J Lumin* 2009, **129**: 1204–1206.

[7]   Wang LL, Cui XJ, Rensberg J, *et al.* Growth and optical waveguide fabrication in spinel $MgGa_2O_4$ crystal. *Nucl Instrum Methods Phys Res B* 2017, **409**: 153–157.

[8]   Goldstein A, Krell A, Burshtein Z. *Transparent Ceramics: Materials, Engineering, and Applications*. John Wiley & Sons, 2020.

[9]   Frage N, Kalabukhov S, Sverdlov N, *et al.* Densification of transparent yttrium aluminum garnet (YAG) by SPS processing. *J Eur Ceram Soc* 2010, **30**: 3331–3337.

[10]   Grasso S, Kim BN, Hu C, *et al.* Highly transparent pure alumina fabricated by high-pressure spark plasma sintering. *J Am Ceram Soc* 2010, **93**: 2460–2462.

[11]   Zhang G, Carloni D, Wu Y. Ultraviolet emission transparent Gd:YAG ceramics processed by solid-state reaction spark plasma sintering. *J Am Ceram Soc* 2020, **103**: 839–848.

[12]   Suzuki T, Murugan GS, Ohishi Y. Spectroscopic properties of a novel near-infrared tunable laser material Ni: $MgGa_2O_4$. *J Lumin* 2005, **113**: 265–270.

[13]   Suzuki T, Hughes M, Ohishi Y. Optical properties of Ni-doped $MgGa_2O_4$ single crystals grown by floating zone method. *J Lumin* 2010, **130**: 121–126.

[14]   Kuleshov N, Shcherbitsky V, Mikhailov V, *et al.* Spectroscopy and excited-state absorption of Ni^{2+}-doped $MgAl_2O_4$. *J Lumin* 1997, **71**: 265–268.

[15]   Sickafus KE, Wills JM, Grimes NW, Structure of spinel. *J Am Ceram Soc* 1999, **82**: 3279–3292.

[16]   O'Neill HSC, Navrotsky A. Simple spinels: Crystallographic parameters, cation radii, lattice energies, and cation distribution. *Am Mineral* 1983, **68**: 181–194.

[17]   Pilania G, Kocevski V, Valdez JA, *et al.* Prediction of structure and cation ordering in an ordered normal-inverse double spinel. *Commun Mater* 2020, **1**: 84.

[18]   Wang P, Yang M, Zhang S, *et al.* Suppression of carbon contamination in SPSed CaF_2 transparent ceramics by Mo foil. *J Eur Ceram Soc* 2017, **37**: 4103–4107.

[19]   Lin FJT, de Jonghe LC, Rahaman MN. Microstructure refinement of sintered alumina by a two-step sintering technique. *J Am Ceram Soc* 1997, **80**: 2269–2277.

[20]   Lin FJT, de Jonghe LC, Rahaman MN. Initial coarsening and microstructural evolution of fast-fired and MgO-doped Al_2O_3. *J Am Ceram Soc* 1997, **80**: 2891–2896.

[21]   Liu L, Zhu Q, Zhu Q, *et al.* Fabrication of fine-grained undoped Y_2O_3 transparent ceramic using nitrate pyrogenation synthesized nanopowders. *Ceram Int* 2019, **45**: 5339–5345.

[22]   Ahsanzadeh-Vadeqani M, Razavi RS, Barekat M, *et al.*, Preparation of yttria nanopowders for use in transparent ceramics by dry ball-milling technique. *J Eur Ceram Soc* 2017, **37**: 2169–2177.

[23]   Naghdi S, Rhee KY, Kim MT, *et al.* Atmospheric chemical vapor deposition of graphene on molybdenum foil at different growth temperatures. *Carbon Lett* 2016, **18**: 37–42.

[24]   German RM. *Sintering Theory and Practice*. Wiley- VCH, 1996.

[25]   Goldstein A, Katz M, Boulesteix R, *et al.* Sources of parasitic features in the visible range of oxide transparent ceramics absorption spectra. *J Am Ceram Soc* 2020, **103**: 4803–4821.

[26]   Wu S, Xue J, Wang R, *et al.* Synthesis, characterization and microwave dielectric properties of spinel $MgGa_2O_4$ ceramic materials. *J Alloys Compd* 2014, **585**: 542–548.

[27]   Wang LL, Liu NQ, Cui XJ. Magnetic and structural

properties of Mg(Ga$_{0.95}$Fe$_{0.05}$)$_2$O$_4$ crystal grown by optical floating zone method. *Mod Phys Lett B* 2020, **34**: 2050245.

[28] Wu S, Xue J, Fan Y. Spinel Mg(Al,Ga)$_2$O$_4$ solid solution as high-performance microwave dielectric ceramics. *J Am Ceram Soc* 2014, **97**: 3555–3560.

[29] Testa-Anta M, Ramos-Docampo MA, Comesaña-Hermo M, *et al.* Raman spectroscopy to unravel the magnetic properties of iron oxide nanocrystals for bio-related applications. *Nanoscale Adv* 2019, **1**: 2086–2103.

[30] Cynn H, Sharma SK, Cooney TF, *et al.* High-temperature Raman investigation of order-disorder behavior in the MgAl$_2$O$_4$ spinel. *Phys Rev B Condens Matter* 1992, **45**: 500–502.

[31] D'Ippolito V, Andreozzi GB, Bersani D, *et al.* Raman fingerprint of chromate, aluminate and ferrite spinels. *J Raman Spectrosc* 2015, **46**: 1255–1264.

[32] Lazarević ŽŽ, Jovalekić Č, Milutinović A, *et al.* Study of NiFe$_2$O$_4$ and ZnFe$_2$O$_4$ spinel ferrites prepared by soft mechanochemical synthesis. *Ferroelectrics* 2013, **448**: 1–11.

[33] Sharma S, Miller JK, Shori RK, *et al.* Schlieren imaging of bulk scattering in transparent ceramics. In: Proceedings of the Solid State Lasers XXIV: Technology and Devices, 2015, **9342**: 93421C.

[34] Morita K, Kim BN, Yoshida H, *et al.* Influence of pre- and post-annealing on discoloration of MgAl$_2$O$_4$ spinel fabricated by spark-plasma-sintering (SPS). *J Eur Ceram Soc* 2016, **36**: 2961–2968.

[35] Jouini A, Yoshikawa A, Brenier A, *et al.* Optical properties of transition metal ion-doped MgAl$_2$O$_4$ spinel for laser application. *Phys Status Solidi C* 2007, **4**: 1380–1383.

[36] Yan S, Wu Z, Xu Q, *et al.* Catalytic reduction of NO$_x$ by CO over a Ni–Ga based oxide catalyst. *J Mater Chem A* 2015, **3**: 15133–15140.

[37] Tauc J, Menth A. States in the gap. *J Non-Cryst Solids* 1972, **8–10**: 569–585.

[38] Jouini A, Yoshikawa A, Guyot Y, *et al.*, Potential candidate for new tunable solid-state laser between 1 and 2 μm: Ni^{2+}-doped MgAl$_2$O$_4$ spinel grown by the micro-pulling-down method. *Opt Mater* 2007, **30**: 47–49.

[39] Yu G, Wang W, Jiang C. Linear tunable NIR emission via selective doping of Ni^{2+} ion into ZnX$_2$O$_4$ (X = Al, Ga, Cr) spinel matrix. *Ceram Int* 2021, **47**: 17678–17683.